University of
Tsukuba Library

Measurement of temperature field of a Rayleigh-Benard convection using two-color laser-induced fluorescence

Measurement of Temperature Field of a Rayleigh-Bénard Convection using Two-Color Laser Induced Fluorescence

by

J. Sakakibara

Institute of Engineering Mechanics and Systems

University of Tsukuba

Tennodai 1-1-1, Tsukuba, 305-8573, Japan.

and

R. J. Adrian

Department of Theoretical and Applied Mechanics

University of Illinois at Urbana-Champaign

Urbana, IL 61801.

abstract

The two-color laser-induced fluorescence technique developed by Sakakibara & Adrian (1999) for the measurement of planar turbulent temperature fields in water has been refined to reduce the rms error of the instantaneous measurement by an order of magnitude. The technique achieves higher sensitivity by employing two high-resolution 14-bit monochrome CCD cameras. Further refinement is achieved by post-processing the data using a convolution method which matches the degree of the image blurring of the two images. The method is demonstrated by application to turbulent Rayleigh-Bénard convection wherein the random error is shown to be less than 0.17K.

List of symbols

B thermal expansion coefficient

C (kg/m^3)   dye concentration

d_B (m) e^{-1} diameter of laser beam

f (m)   focal length

g (m/s^2)   gravitational accelration

G point spread function

I fluorescent intensity without background intensity, $I = \tilde{I} - I_b$

I_b background intensity

I_c corrected intensity

I_s intensity of fluorescence excited by stationary laser beam

$\tilde{I}$ light intensity deteced by CCD cameras

ΔI absorbed light intensity

k (m^2/s)   thermal diffusivity

Pr   Prandtl number

Q_0 (mK/s)   kinematic heat flux at lower (and upper) surface.

Ra   Rayleigh number

T (K)   temperature

T_0, T_1 (K)   temperature for reference images

T_L (K)   temperature of lower surface

T_U (K)   temperature of upper surface

T_{RMS} (K)   RMS temperature

T_b (K)   mean temperature at mid-height of cell

$\bar{T}$ (K)   mean temperature

ΔT (K)   temperature difference between upper and lower surface, $\Delta T = T_L - T_U$

Δt (s)   time period of excitation against local fluorescent molecule, $\Delta t = d_B/V_s$

V_s (m/s)   beam speed in vertical direction

w_* (m/s)   Deardorff's velocity scale, $w_* = (gBQ_0 z_*)^{1/3}$

X (pixel)   image coordinate (horizontal)

x (m)   physical coordinate (horizontal)

Y (pixel)   image coordinate (vertical)

z (m)   physical coordinate (vertical)

z_* (m)   layer half-depth

ϵ (m^2/kg)   absorption coefficient of dye

ϕ quantum yield

γ ratio of fluorescent intensities at each pixel location

γ_0, γ_1 ratio of fluorescent intensities at $T = T_0$ and $T = T_1$, respectively

κ (1/K)   temperature sensitivity

λ_R (m)   reflected wavelength of beam splitter

λ_T (m)   transmitted wavelength of beam splitter

λ_{abs} (m)   wavelength yielding maximum absorption

λ_{em} (m)   wavelength yielding maximum emission

λ_{ex} (m)   wavelength of laser beam

ν (m^2/s)   kinematic viscosity

θ_* (K)   Deardorff's temperature scale, $\theta_* = Q_0/w_*$

σ_{I} noise level of intensity averaged over 10 by 10 pixels

σ_γ noise level of intensity ratio, $\sigma_\gamma = (2\sigma_{\mathrm{I}}^2)^{1/2}$

σ_{T} (K)   standard deviation of measured temperature

ξ coefficient for mapping function (X)

η coefficient for mapping function (Y)

Subscripts and superscripts:

RhB   Rhodamine B

Rh110   Rhodamine 110

α camera α for Rhodamine B

β camera β for Rhodamine 110

1 Introduction

This paper describes a measurement of the temperature field of Rayleigh-Bénard convection in water on planar domains using two-color laser induced fluorescence.

Temperature-sensitive fluorescent dyes excited by laser light can be used as a temperature diagnostic (Nakajima *et al.* 1990; Sakakibara *et al.* 1993 & 1997; Satoh & Kasagi 1997; Lemoine *et al.* 1999; Coolen *et al.* 1999). Here, the fluorescence intensity is proportional to the exciting light intensity and the concentration of the fluorescent dye. For some dyes, e.g., Rhodamine B, the fluorescence intensity depends on the temperature. This characteristic can be used to measure the temperature of a solvent if both the concentration and the exciting light intensity can be kept constant. In practice, however, the exciting light intensity may vary due to several effects, including refraction of the light passing through the thermal field itself. This may cause significant error in the measurement. In order to overcome this problem, a two-color LIF technique which employs two fluorescent dyes whose emission intensities depend differently upon temperature was developed by Sakakibara & Adrian (1999). The ratio between the two fluorescence intensities is nearly independent of the incident light intensity. Kim & Kihm (2003) applied the two-color LIF technique to the temperature measurements in a micro-scale heated channel. A similar technique was developed by Coppeta & Rogers (1998). Their technique, called dual emission LIF, was capable of measuring temperature and PH distribution in aqueous fluid simultaneously. Lavieille *et al.* (2001) developed two colors/one dye LIF, which employs two different spectral bands each having temperature sensitive and non-sensitive emissions.

In this paper, we apply the two-color LIF technique to the measurement of temper-

ature in high aspect-ratio Rayleigh-Bénard convection, which is thermal convection in a horizontal layer of fluid heated from below and cooled from above. Digital CCD cameras with 14 bit resolution were employed in order to improve the accuracy of the measurements. Also a convolution technique was developed in order to match the degree of the image blurring of the two images, and striations were successfully removed in the temperature distributions. Establishment of this new convolution technique and the use of higher resolution cameras express the further development of our work relative to that described in our previous paper (Sakakibara & Adrian 1999).

2   Method

2.1   Flow Apparatus

Figure 1 shows the Rayleigh-Bénard convection cell. The x axis denotes a horizontal direction, and the z axis denotes the vertical direction. The platform dimension is 914 mm × 914 mm, and the layer depths is $2z_* = 120$ mm. As same as our previous work (Sakakibara & Adrian 1999), the working-fluid was de-ionized water containing Rhodamine B (RhB) and Rhodamine 110 (Rh110) that are temperature-sensitive and non-temperature-sensitive fluorescent dyes, respectively. The basic characteristics of RhB and Rh110 in water at $T = 20°C$ are summarized in Table.1.

The concentrations of the fluorescent dyes have to be as low as possible, in order to reduce the error due to the absorption of light (see §3). The lower concentration, however, leads to a lower fluorescent light intensity, and consequently to a lower signal to noise ratio of the fluorescent images, if the excitation light intensity is not sufficiently high. In this study, the concentration of each dye, RhB and Rh110, was set at $C_{RhB} = 0.0055 \text{mgl}^{-1}$

7

and $C_{\text{Rh110}} = 0.0011 \text{mgl}^{-1}$, respectively. With this concentration and the optical setup described in §2.2, the effect of absorption is considerably small (§3), while the fluorescence intensity was high enough to maximize the S/N ratio of the images captured by the cameras.

The layer was heated from below by four identical square (457.2 mm × 457.2 mm) etched-foil resistance heating mats (Watlow), which were bonded to the bottom of a 25.4 mm thick aluminum plate. The current for each heater was supplied by one of four identical 2.5kW DC power supplies (TCR 200S14-2-D, Electronic Measurements). The layer was cooled from above by a 76.2 mm thick aluminum plate that has rectangular aluminum cooling water channels attached to its upper surface.

The side walls of the test section were made from polycarbonate with glass inserts for optical access. In order to minimize cooling due to conduction through the side walls, they were insulated using a 6 mm air gap and an extra pane of 3 mm-thick glass. A cylindrical 0.8 mm-thick polycarbonate interior window with a diameter of 760 mm was used in order to provide additional insulation and to further isolate the temperature field from the rectangular side walls. In particular, the cylindrical wall eliminated any preferred direction, and reduced the likelihood of the large-scale flow locking into a single orientation for a long period of time compared with the large-scale turnover time. With the cylindrical window in place, the aspect ratio of the cell was 6.3:1.

The Rayleigh number was set at Ra= $gB\Delta T \left(2z_*\right)^3 /k\nu = 4.5 \times 10^8$. Here, g is gravitational acceleration, B is the thermal expansion coefficient, $\Delta T = T_{\text{L}} - T_{\text{U}}$ is the temperature difference between the upper (T_{U}) and lower (T_{L}) surface, k is the thermal diffusivity and ν is kinematic viscosity. The characteristic velocity and temperature scales, known as Deardorff's scale (Deardorff 1970), are defined as $w_* = \left(gBQ_0z_*\right)^{1/3}$ and $\theta_* =$

8

Q_0/w_*, respectively, where Q_0 is the kinematic heat flux at the lower (and upper) surface. The experimental parameters and scales are summarized in Table 2. All parameters and scales are calculated using the thermophysical properties of water at the temperature T_b measured at the mid-height of the cell.

The temperature uniformity of the lower plate was measured by means of nine surface-mounted thermocouples (Fernandes & Adrian 2001). The temperatures were found to be spatially uniform within 0.2 K peak-to-peak. The temperature distribution in the top plate was measured by the thermocouples mounted in holes drilled from the top of the plate to within 10 mm of the lower surface of the plate. The mean temperature had a spatial variation of 0.13 K peak-to-peak with a standard deviation of 0.05K.

2.2   Optical Configuration

The optical system consisted of transmitting and receiving parts shown schematically in Fig.2. A rectangular planar region-of-interest (ROI), having a dimension of 160 mm in the horizontal direction and 120 mm in the vertical direction, was first determined to be located through the center axis of the test section.

In the transmitting part, a laser beam having a wavelength of λ_{ex}=488 nm and light power of 0.6 W was emitted from an Argon-ion laser (Innova70, Coherent). The maximum emission wavelength of Rhodamine 110 is 520 nm, while the green line of an Argon-ion laser is 514.5 nm, making these wavelengths difficult to separate. Thus we used 488 nm for the excitation instead of 514.5 nm. The laser beam was then swept cyclically in the vertical direction from the bottom to the top by a scanning mirror (6325D, General Scanning) connected with a scanner controller (CX660, General Scanning) in order to form a laser light sheet in the ROI. The scanner controller was triggered by a PC through

9

Table 1: Basic characteristics of RhB and Rh110. Solvent was deionized water, $T = 20°C$.

*Arbeloa *et al.*(1991), **Jones (1990).

Dye	Molecular weight	λ_{abs} [nm]	λ_{em} [nm]	ϕ	$\epsilon_{\lambda=488}$ [m^{2}g^{-1}]	$\epsilon_{\lambda=\lambda_{\text{RhB}}}$ [m^{2}g^{-1}]	$\epsilon_{\lambda=\lambda_{\text{Rh110}}}$ [m^{2}g^{-1}]
RhB	479.02**	554	575	0.31*	4.4	1.1	5.8
Rh110	366.80**	496	520	0.8	34	0.073	1.1

Table 2: Experimental parameters and scales.

Ra	4.5×10^8
Nu	40.9
Pr	6.54
ΔT	12.1 K
T_b	$23.0°C$
Q_0	0.611 K mm s^{-1}
z_*	60.0 mm
w_*	4.6 mm s^{-1}
θ_*	0.13 K

the digital I/O interface attached to a frame grabber, as explained below. The beam speed in the vertical (sweep) direction at the center of the cell, where the ROI was located, was approximately $V_s = 120$ mm/s.

Due to the finite beam speed V_s, the measured temperature distribution during a scan could be slightly distorted compared to a true instantaneous distribution. This distortion of the temperature distribution can be characterized by a ratio of the velocity scale and the beam speed, w_*/V_s. In the present study, $w_*/V_s = 0.038$, which is small enough to allow discussion of the topology of the thermal structures.

The e^{-1} diameter of the light beam at the ROI was $d_B = 1.4$ mm. Thus, the time period of excitation against local fluorescent molecule was $\Delta t = d_B/V_s = 0.012$ s, and displacement of the fluid in this period, expressive of the degree of smearing of fluorescent image, was $w_*\Delta t = 0.055$ mm.

One could have produced a cylindrical-lens-expanded light sheet instead of using the scanning beam. In that case, however, the light intensity is distributed non-uniformly (i.e., Gaussian form) and thus the S/N ratio varies significantly over the measurement region, unless lenses are used which are specially designed to give a top-hat profile by varying the index of the refraction of the glass. Further more, the local light flux of cylindrical-lens-expanded light sheet would be much smaller than that of a scanned beam. Thus, a longer duration of excitation against individual fluorescent molecule would be required in order to capture the fluorescent images with the same S/N ratio. The longer duration of excitation, however, would cause blurring of images and small scale thermal structures would be smeared out. This is not a problem with the scanning beam.

In the receiving optics, the fluorescent light emitted from the fluorescent molecule in the ROI was split by a dichroic beam splitter (SWP-45-R570-T520-PW2025C, CVI).

11

At a 45 degree incident angle the beam splitter transmitted wavelengths $\lambda_T \leq 520$nm and reflected the wavelengths $\lambda_R \geq 570$nm. Between these limits the transmittance and reflectance varied continuously. The transmitted light was passed through a filter that rejected wavelengths lower than 495nm (03FCG067, Melles Griot) in order to eliminate the Rayleigh and Mie scattering from particles in the flow. The light was then collected by a lens (Nikkor $f = 50$mm, F1.2, Nikon) and imaged onto a CCD camera β (KX85, 1300 pixels $\times$ 1030 pixels $\times$ 14 bits, Apogee). The reflected light was also passed through a filter that rejected wavelengths shorter than 570 nm (03FCG089, Melles Griot) in order to eliminate the shorter wavelengths completely. It was imaged onto the other CCD camera α, which is identical to the CCD camera β with same lens. So, the CCD cameras α and β detected mainly the images of RhB and Rh110 emissions, respectively. The position of each CCD camera was adjusted to capture the images of approximately the same area in the ROI. Since we calibrated the physical co-ordinates and the image co-ordinates (see §2.3), more precise positioning of the cameras was not needed.

The image signal from CCD cameras were then transferred to the PC's host memory via ISA bus digital frame grabbers supplied by the manufacturer of the camera. The camera exposure and the beam scan were started simultaneously by triggering both the frame grabber and the scanner controller. The exposure time was set to 1.0 s which is identical to the time duration of the entire scan of the beam. The interval between successive exposure frames was approximately 4.0 s, which was the shortest frame interval we could realize using the current frame grabber. The distance between the front head of the lens and ROI plane was 1070 mm.

2.3 Calibration of Image Coordinates

To determine the correspondence between physical coordinates and image coordinates, we took images of a calibration plate, which was prepared to have an equally-spaced grid pattern at 2 mm intervals on its surface. A dot was drawn at the center of the plate as a reference point, and the relative position of the reference point was measured prior to the calibration. The surface of the plate was carefully set in the plane of the laser light sheet and illuminated from the front by a halogen lamp. The grid image was captured by each CCD camera through the receiving optics. The location of each grid point in the image plane coordinates was obtained automatically by finding the local peaks of a cross-correlation function between the grid image and a template image which had a pattern of one grid. After obtaining the correspondence between the location of each grid point in the physical coordinate and that in the image coordinate, a 3rd-order polynomial function was created as a mapping function from the physical coordinate (x, z) to the image coordinate (X, Y)

$$X = \sum_{i=0}^{3}\sum_{j=0}^{3} \xi_{ij} x^i z^j, \tag{1}$$

$$Y = \sum_{i=0}^{3}\sum_{j=0}^{3} \eta_{ij} x^i z^j, \tag{2}$$

where $\xi_{ij} = \eta_{ij} = 0$ for $i+j > 3$. The coefficients ξ_{ij} and η_{ij} were obtained by the least-square method. This procedure compensated automatically for camera mis-alignment and distortion due to refraction by the liquid interfaces. A similar procedure is discussed in detail in reference (Solof *et al.* 1997).

2.4 Image Processing

An example of the fluorescence image is shown in Fig.3. The gray level represents the magnitudes of $\tilde{I}^{\alpha}(x, y)$ and $\tilde{I}^{\beta}(x, y)$, which are the light intensities deteced by CCD cameras α and β, respectively. Here, the original image directly captured by CCD cameras has been transformed into physical coordinates using the mapping function eqs.(1) and (2). In this transformation, a bi-linear interpolation scheme was used to obtain intensities at sub-pixel locations. The interval between each pixel of this transformed image is almost the same as that of the original image directly captured by CCD camera. Hereafter, the term 'pixel' refers to the pixel in this transformed image, not the pixel in the original image.

Several left-right striations running through the ROI are caused by the refraction of the laser light beam in the fluid's irregular density before the light enters the ROI. Temperature-dependent fluorescent intensity variations, such as thermal structures, are not visible by naked eye in these images.

The ratio of fluorescent intensity at each pixel location was computed from the above 'raw' images by a form,

$$\gamma = \frac{I^{\alpha}}{I^{\beta}}, \tag{3}$$

where

$$I^{\alpha} = \tilde{I}^{\alpha} - I_{b}^{\alpha}, \tag{4}$$

$$I^{\beta} = \tilde{I}^{\beta} - I_{b}^{\beta}. \tag{5}$$

I_{b} is background intensities at each pixel location measured without illuminating the laser light.

Two sets of reference images having uniform known temperatures T_0 and T_1 need to

be captured before or after taking images of the flow field to be measured. The ratio of intensities for the reference images are then denoted as $\gamma_0 = \gamma|_{T=T_0}$ and $\gamma_1 = \gamma|_{T=T_1}$. Thus, the temperature was determined in terms of the linear interpolation

$$T = \gamma \frac{T_1 - T_0}{\gamma_1 - \gamma_0}. \tag{6}$$

General speaking, the ratio of fluorescence intensities, γ, is not proportional to temperature. However, we did not use a higher order calibration curve such as exponential or polynomial functions, because the temperature range of interest is not very large, e.g., the temperature variation in the thermal plume of our study was typically $T_b \pm 2.0$K or less. Within this temperature range, the maximum and minimum bias error due to the linear approximation of the calibration curve was estimated as +0.13K and -0.05K, respectively.

Note that the temperature sensitivity, $\kappa \left(= (\gamma_1 - \gamma_0) / (T_1 - T_0)\right)$, was $\kappa = 1.38\%$/K at $T = 25.4°C$ under the current optical configuration and concentration ratio of the fluorescent dyes.

Figure 4(a) shows a temperature distribution computed from the images shown in Fig.3. The thermal structures are now visible; hot plumes are represented by white color rising upward from the bottom surface and cold plumes by black falling downward from the top surface. Since the ratio of intensities would not depend on the exciting light intensities, the striations in the original images were expected to be canceled off. However, the striations are still not completely eliminated and the 'temperature' error due to them is almost as intense as the plume temperatures.

This was caused by a difference of the image blurring between two images. This is obvious in Fig.5, which shows a profile of the fluorescence intensity and its ratio in Y direction, i.e., cross-striation direction, where a stationary laser light beam excited the

fluorescence having uniform temperature. Both intensity profiles were expected to be matched completely, but, in reality, both profiles are slightly different in shape, and, therefore, the ratio is not constant although the temperature was uniform. Disagreement of the shape of the profiles might have originated from the different focusing and aberrations of the object lens, or from astigmatic aberration caused by the inclined plate beam splitter. Instead of eliminating hardware aberrations or defocusing, a software correction of the images was performed to match both profiles, or both image blurrings. Consider I_c^α as an intensity profile corrected from I^α and having a profile exactly the same as that of I^β. Defining G as a linear transfer function, or point spread function, which transforms I^α to I_c^α,

$$I_c^\alpha = I^\alpha \otimes G, \tag{7}$$

where $\otimes$ denotes a convolution operation. According to Parceval's theorem, the convolution can be rewritten in a product of Fourier transform of functions,

$$\mathcal{F}(I_c^\alpha) = \mathcal{F}(I^\alpha) \cdot \mathcal{F}(G), \tag{8}$$

where $\mathcal{F}$ denotes a Fourier transform. Thus, the I_c^α can be obtained as

$$I_c^\alpha = \mathcal{F}^{-1}\left(\mathcal{F}(I^\alpha) \cdot \mathcal{F}(G)\right), \tag{9}$$

where $\mathcal{F}^{-1}$ denotes an inverse Fourier transform. This operation was performed for the entire images, and the intensity ratio was then computed by

$$\gamma = I_c^\alpha / I^\beta. \tag{10}$$

In order to obtain the transfer function G, the stationary laser light beam was inserted in the flow field having uniform temperature, and its fluorescent images were captured

16

prior to the actual measurement. Intensity profile of fluorescent light excited by the stationary laser light beam, I_s^α and I_s^β, needs to be equated by the transfer function G by

$$I_s^\beta = I_s^\alpha \otimes G. \tag{11}$$

Applying the Fourier transform, the transfer function G can be obtained as

$$\mathcal{F}(G) = \frac{\mathcal{F}(I_s^\beta)}{\mathcal{F}(I_s^\alpha)}. \tag{12}$$

Several images for the stationary beam having various vertical locations were obtained in order to establish the transfer function G at many location in the image coordinate, since the degree of aberration or defocusing are not uniform in the whole region of the image and operations of eq.(9) and eq.(12) have to be performed locally in the image. The number of pixels to establish G was chosen to be 128 pixels vertically located in a line centered on the laser light beam.

By applying eq.(9),(10), and (6) on the images displayed in Fig.3(a) and Fig.3(b), the temperature distribution was computed as shown in Figure 4(b). Now, the striations are completely eliminated without adding any additional noise or deformation to the data.

We should note that the result was different and unsuccessful when we tried to correct I^β instead of I^α. Since the image I^β was more blurred than I^α, the point spread function G actually acted as a differentiation operator to sharpen the image I^β. As a result, the convoluted image I_c^β had high frequency noise, which made the measured field much noisier than without convolution.

After removing the striations, the measured temperature for each location was spatially averaged with others over 10 by 10 points $(1.2 \times 1.2\text{mm}^2)$ in order to reduce random noise. Note that the RMS value of the electrical noise contained in the intensity signal coming from the each pixel element of the present CCD camera was approximately 1.4% of the

signal level. This noise was reduced to $\sigma_I = 0.14\%$ after averaging over 10 by 10 pixels. This fact implicitly means that the noise signals of any two different pixels are uncorrelated without any fluctuating bias of multiple pixels.

3   Error Estimates

To examine the random error of the measurement, a flow field having uniform temperature with perturbation of the excitation light intensity was measured by the present system. A small glass container ($150 \times 150 \times 150\text{mm}^3$) with an aluminum bottom and columns at the corners was placed on the bottom surface of the Rayleigh-Bénard convection cell. The center of the ROI was set at the center of the container. Thin Styrofoam blocks were mounted between the glass container and the cell's bottom surface in order to reduce the heat conduction from the cell to the container. The container was filled with fluid and dyes in the same manner as in the cell. By adding heat to the bottom surface of the cell, convection in the cell was established, while the fluid inside the container still had much weaker convection and the temperature was almost uniform. The laser light sheet that traveled through the cell was refracted and created unsteady striations in the ROI plane in the same manner as the one for the real measurement. The LIF data obtained at the mid-height of the cell shows that the standard deviation of the measured temperature was σ_T=0.17K for the present method with the blurring correction, and 0.20K without the correction. This error is smaller than that of the previous works of Sakakibara & Adrian (1999) and Kim & Kihm (2002), who reported were ±1.4K and ±1.5K with 95% confidence, respectively. Such an improvement of accuracy in the present study was due mainly to the use of a 14-bit camera, and additional improvement was achieved by means

of the blurring correction technique.

One of major sources of error originated from the CCD camera's noise. Since the ratio of intensity was obtained from two independent CCD cameras each having the noise σ_I, the noise in the intensity ratio is $\sigma_\gamma = (2\sigma_\mathrm{I}^2)^{1/2}$. Thus the error due to the CCD noise can be estimated as $\sigma_\gamma/\kappa = 0.14K$.

Coppeta and Rogers (1998) pointed out the effect of the spectral conflict, which is an overlap between absorption and emission bands. They classified spectral conflict into three types. The type I conflict is an overlap between the emission bands of each dye. As the degree of this conflict increases, the temperature sensitivity κ decreases. This effect is already reflected in the value of κ and the above measurement error σ_T. The type II conflict is an overlap between the emission band of one dye and the absorption band of a second dye where the absorption band of the second dye does not change with changes in the scalar being measured. In the present case, the fluorescence light emitted from Rhodamine 110 might be absorbed when it travels through the dye Rhodamine B before being measured. The absorbed light intensity ΔI normalized by the emitted light intensity I can be written as

$$\frac{\Delta I}{I} = 1 - e^{-\epsilon Cl}, \tag{13}$$

where ϵ is the absorption coefficient of Rhodamine B at the wavelength of Rhodamine 110 emission, which is $\epsilon = 5.8\mathrm{m}^2\mathrm{g}^{-1}$ (refer $\epsilon_{\lambda=\lambda_{\mathrm{Rh}110}}$ in Table 1), C is the concentration of Rhodamine B, and l is the travel distance from the ROI to the front window of the test section, which is 457 mm (half the size of the Rayleigh-Bénard cenvection cell) from the center of the ROI. In the type II conflict, ϵ and C are considered to be constant and only a variation of l is important. If l is constant over the measurement region, the sensitivity κ is constant and causes no error due to type II conflict. However, l has a small amount

of variation due to view angle. The variation of the travel distance l of the present case was estimated to be $\Delta l = 0.0032l$ based on a simple geometrical analysis. Thus a change of $\Delta I / I$ in terms of the variation of l is expressed as

$$\frac{\Delta I \left(l + \Delta l\right)}{I} - \frac{\Delta I \left(l\right)}{I} = e^{-\epsilon Cl} - e^{-\epsilon C(l+\Delta l)} = 4.6 \times 10^{-5}, \tag{14}$$

which leads to a temperature error of 0.0033 K, by simply dividing the above value by κ.

The final type of spectral conflict, the type III conflict, is an overlap between the emission band and the absorption band which do change in the scalar being measured. In the present case, the variation of the absorption coefficient ϵ in eq.(13) should be considered. The temperature sensitivity of the absorption coefficient is less than 0.05 %/K (Sakakibara & Adrian 1999). Thus the variation of ϵ can be estimated as $\Delta \epsilon = 0.0005\Delta T \epsilon = 0.035 \mathrm{m}^2 \mathrm{g}^{-1}$. Then, a change of $\Delta I / I$ in terms of the variation of ϵ is expressed as

$$\frac{\Delta I \left(\epsilon + \Delta \epsilon\right)}{I} - \frac{\Delta I \left(\epsilon\right)}{I} = e^{-\epsilon Cl} - e^{-(\epsilon+\Delta\epsilon)Cl} = 8.7 \times 10^{-5}, \tag{15}$$

which leads to a temperature error of 0.0063 K, by simply dividing the above value by κ. It is now clear that the error due to the type II and type III spectral conflicts in the present case is considerably small compared to the other errors mentioned previously in this section. Note that this error would be larger if the concentration of Rhodamine B was higher.

4   Results

Statistics were calculated from 2820 instantaneous temperature maps measured over experiments which were run continuously for over 5 hours. Figure 6(a) shows the mean temperature profile. Typical features of Rayleigh-Bénard convection, such as a steep slope near the wall and flat plateau in the middle of layer, are well captured. Deviation in the flat plateau region, which is not expected physically, is approximately ±0.2K which can be recognized as the bias error of the present measurement. An RMS temperature profile shown in Fig.6(b) is overlaid with the results obtained by thermocouple measurements performed using the same apparatus by Fernandes & Adrian (2001). While both agree well in the region close to the wall, a deviation is obvious in the middle of layer where the temperature fluctuation is smaller. The random error in LIF measurement would tend to increase the measured variance, and since the random error is independent of temperature, its effect will be greater at lower temperatures. Note that the measurement volume of LIF was 1.2 mm × 1.2 mm × 1.4 mm, and the diameter of the thermocouple probe was 0.3 mm.

Figure 7 shows probability density functions for temperature. The PDF at the mid height ($z/z_* = 1.0$) is symmetric but slightly wider than that reported by Fernandes & Adrian (2001) in which the PDF exhibited clear exponential form (shown in dashed lines). This disagreement is due to the random error which adds additional fluctuation of 'measured temperature'. The distributions shown by measurements at probes located off center are skewed and have tails in the direction of the nearest wall. This is because of the occasional temperature drop (rise) due to plumes. PDF reported by Belmonte *et al.* (1994), who performed measurements in a cubic cell at Ra= 4.8×10^7 for air, shows the

same qualitative features.

Instantaneous temperature distributions are presented in Fig.8. We made several observations which described different aspects of the plume structures. Figures 8(a) and (b) have relatively small plumes like mushrooms of less than $0.5z_*$ in visual height. The region at mid-height of the cell has no clear structures, and the plumes in the upper and lower plates show no interactions. Note that the temperatures of typical plumes are within a range of $T_b \pm 2\mathrm{K}$.

Plumes grows further exhibiting medium size plumes shown in Fig.8(c) and (d). The plumes are larger in vertical length and extend from the bottom plate to a height larger than $z/z_* = 0.5$. The plume's heads are not clear as in the mushrooms and their edges are smeared due to diffusion.

The largest plumes are observed in Fig.8(e) and (f). In both figures, the entire region was filled with hot plumes rising from the bottom plate, and the heads of some hot plumes penetrated close to the upper boundary layer. The fluid driven by the packet of the plumes flows toward the upper plate, where the cold plumes cannot be grown, and its boundary layers were made thinner. This packet of rising plumes is expected in the edge of the large-scale roll-cells, which has been previously visualized (Keane 1993) as irregular polygons resembling the Bénard hexagon observed in low-Reyleigh-number convection. The small-scale plumes are embedded on these large-scale roll-cells (Sparrow *et al.* 1970; Chu and Goldstein 1973). Fernandes & Adrian (2001) reported that the vertical sections through the roll-cells encompass the layer-depth $2z^*$, which is comparable to the largest plumes observed here. Note that the horizontal cell-width reported by Fernandes & Adrian (2001) is approximately $3.6z_*$, which is larger than the horizontal size of the measurement region in this study.

Figure 8(g) and (h) shows medium-sized tilting plumes. The direction of the rising plumes on the top and bottom sides are almost parallel, indicating a large-scale circulation spanning the entire height of the cell. Here, a horizontal mean flow toward the right (left) on the bottom (top) surface tilts the plumes in that direction. This circulation might be caused by the large-scale roll-cell mentioned above, and the plane of the pictures being in the middle of the cell.

5   Conclusion

The two-color laser-induced fluorescence technique was applied to the measurement of the planar distribution of temperature in Rayleigh-Bénard convection in a high aspect-ratio cell. Rhodamine B and Rhodamine 110 were used as temperature-sensitive and non-temperature-sensitive indicators, and 14-bit digital CCD cameras were employed to achieve a greater level of accuracy in comparison to the results of previous measurements. Striations in the ratio of two fluorescent images occurred due to a different blurring of the light through the imaging optics were successfully removed by new convolution technique which matches the degree of the image blurring of the two images. The accuracy of temperature measurement was then 0.17K defined as a standard deviation of the measured temperature of a fluid having uniform temperature with fluctuating laser light sheet illumination. The RMS temperature profile and probability density functions of the Rayleigh-Bénard convection agreed closely with the previous measurement obtained by means of a thermocouple. The instantaneous temperature distributions provide several representative structures of buoyant plumes.

6 Acknowledgments

References

[1] Arbeloa, T.L.; Estevez, M.J.T.; Arbeloa, F.L.; Aguirresacona, I.U.; Arbeloa, I.L. 1991: Luminescence properties of rhodamines in water/ethanol mixtures. J. Luminescence 48 & 49, 400-404

[2] Belmonte, A.; Tilgner, A.; Libchaber, A. 1994: Temperature and velocity boundary layers in turbulent convection. Phys. Rev. E 50, 269-281

[3] Coolen, M.C.J.; Kieft, R.N.; Rindt, C.C.M.; van Steenhoven A.A. 1999: Application of 2-D LIF temperature measurements in water using a Nd:YAG laser. Exp. Fluids 27, 420-426

[4] Coppeta, J.; Rogers, C. 1998: Dual emission laser induced fluorescence for direct planar scalar behavior measurements. Exp. Fluids 25, 1-15

[5] Deardorff, J.W. 1970: Convective velocity and temperature scales for the unstable planetary boundary layer and for Rayleight convection. J. Atmosph. Sci. 27, 1211-1213

[6] Fernandes, R. L. J.; Adrian, R. J. 2001: The spatial structure of turbulent Rayleigh-Bénard convection. Ph.D thesis, Department of Theoretical and Applied Mechanics, University of Illinois at Urbana-Champaign.

[7] Jones, G. II, 1990: Photochemistry of laser dyes. Dye Laser Principles with applications (Ed. Duarte F.J.; Hillman, L.W.) 287-343. Academic Press

[8] Keane, R. D. 1993: A theoretical and computational investigation to optimize particle image velocimetry and study of thermal convection from non-uniform surface. Ph.D

thesis, Department of Theoretical and Applied Mechanics, University of Illinois at Urbana-Champaign.

[9] Kim, H.J.; Kihm, K.D.; Allen, J.S. 2003: Examination of ratiometric laser induced fluorescence thermometry for microscale spatial measurement resolution. Int. J. Heat Mass Transf. 46 (21), 3967-3974

[10] Lavieille, P.; Lemoine, F.; Lavergne, G.; Lebouche, M. 2001: Evaporating and combusting droplet temperature measurements using two-color laser-induced fluorescence. Exp. Fluids 31, 45-55

[11] Lemoine, F.; Antoine, Y.; Wolff, M.; Lebouche, M. 1999: Simultaneous temperature and 2D velocity measurements in a turbulent heated jet using combined laser-induced fluorescence and LDA. Exp. Fluids 26, 315-323

[12] Nakajima, T.; Utsunomiya, M.; Ikeda, Y.; Matsumoto, R. 1990: Simultaneous measurement of velocity and temperature of water using LDV and fluorescence technique. Proc. 5th Int. Symp. on Appl. of Laser Tech. to Fluid Mech.,Lisbon, 2.6.1-2.6.6

[13] Sakakibara, J.; Hishida, K.; Maeda, M. 1993: Measurements of thermally stratified pipe flow using image-processing techinques. Exp. Fluids 16, 82-96

[14] Sakakibara, J.; Hishida, K.; Maeda, M. 1997: Vortex structure and heat transfer in the stagnation region of an impinging plane jet (simultaneous measurement of velocity and temperature fields by DPIV and LIF). Int. J. Heat Mass Transfer 40, 13, 3163-3176

[15] Sakakibara, J.; Adrian, R.J. 1999: Whole field measurement of temperature in water using two-color laser induced fluorescence. Exp. Fluids 26, 7-15

[16] Sato, K.; Kasagi, N.; Suzuki, Y. 1997: Combined velocity and scalar field measurement with the simultaneous use of PIV and scanning LIF. Proc. 10th Int. Symp. Transport Phenomena in Thermal Science and Process Engineering, Kyoto, Vol.2, pp. 541-546

[17] Solof, S.M., Adrian, R.J., Liu, Z-C. (1997) Distortion compensation for generalized stereoscopic particle image velocimetry. *Measurement Science and Technology* 8: 1441-1454
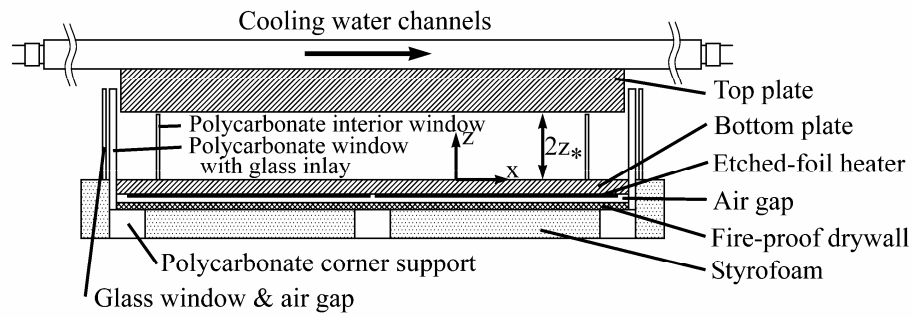
Figures

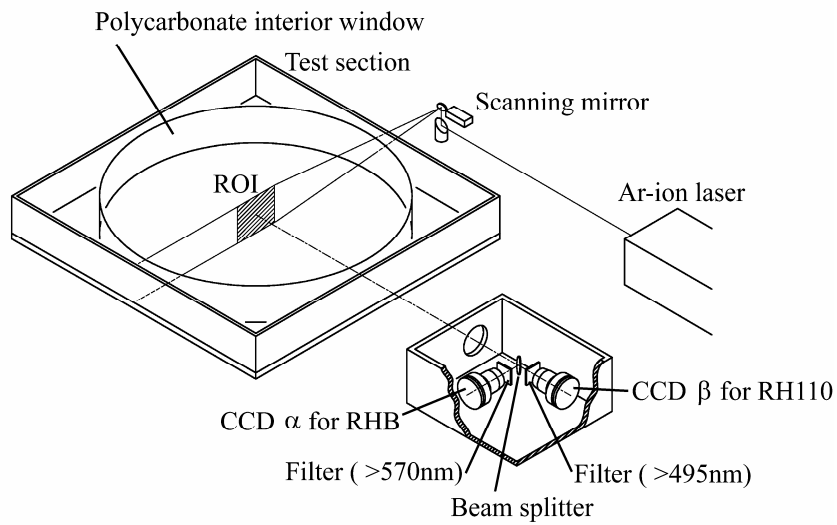Figure 1: Schematic of Rayleigh-Bénard convection cell.

Figure 2: Arrangement of transmitting and receiving optics. The top plate of the test section is not illustrated.
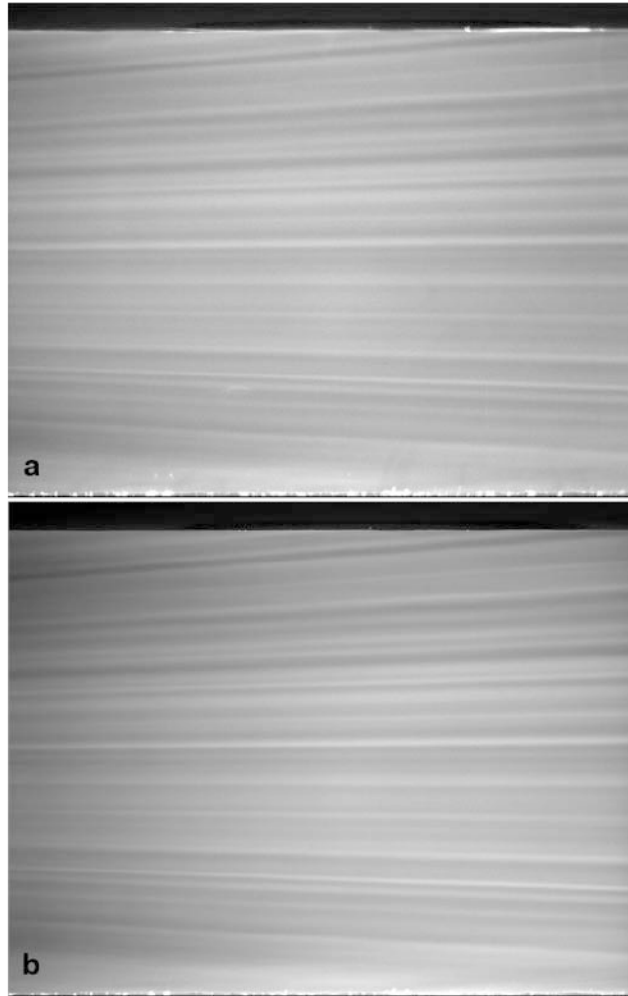
Figure 3: Fluorescent images captured by individual CCD cameras; (a) Camera α (Rhodamine B), (b) Camera β (Rhodamine 110).
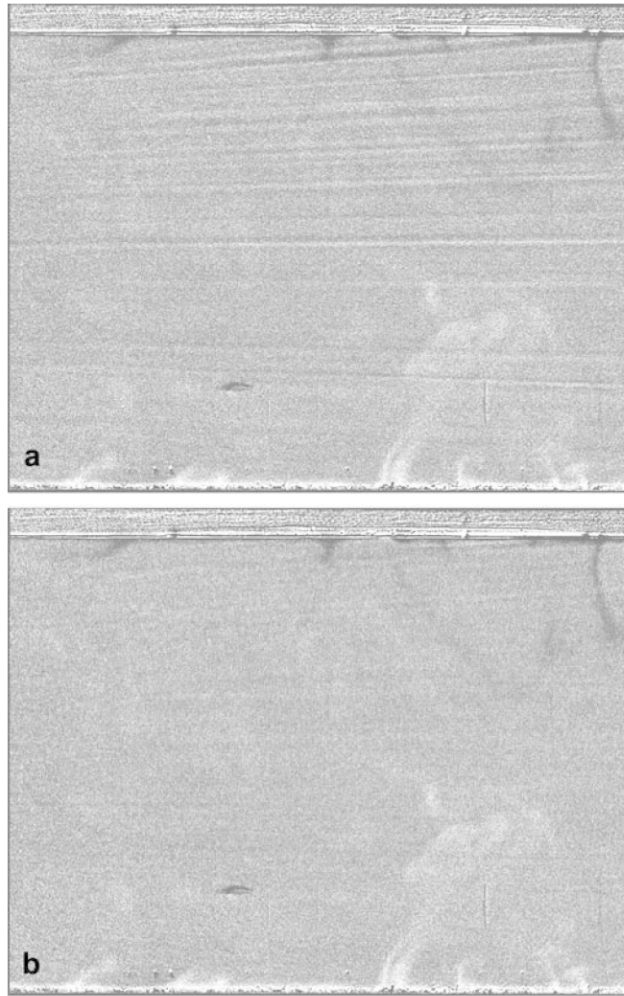
Figure 4: Ratio of fluorescence intensity; (a) without blurring compensation, (b) with blurring compensation.
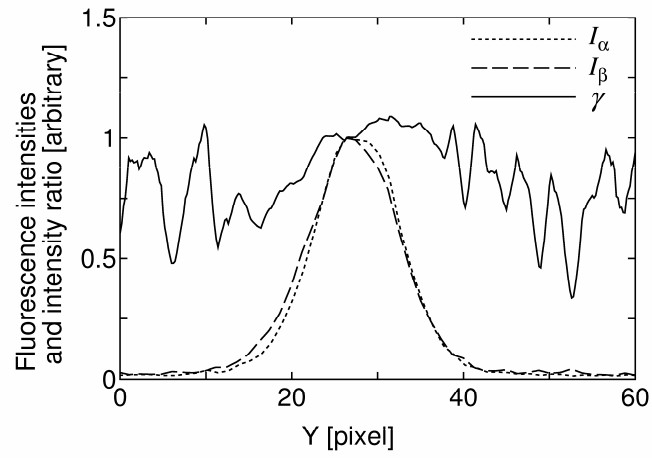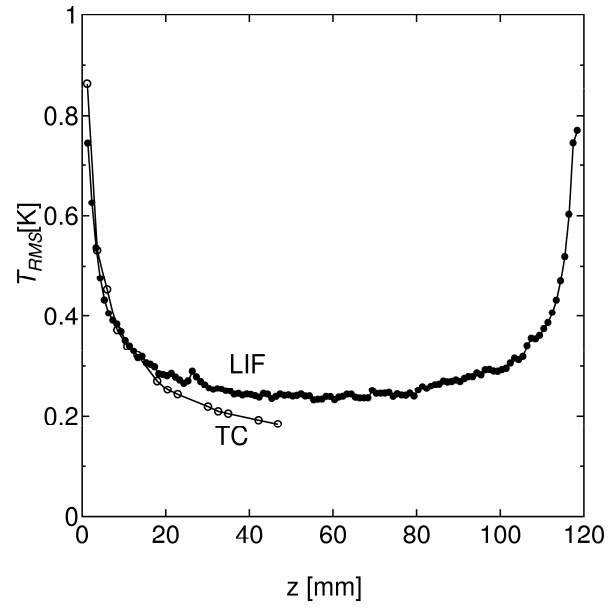
Figure 5: Fluorescence intensity distribution and their ratio across the laser light beam. Rhodamine 110 distribution is slightly wider than that of Rhodamine B.

Figure 6: Mean temperature (a) and RMS temperature (b) distibutions.

Figure 7: Probability density function for temperature.

Figure 8: Instantaneous temperature distributions.

Cooling water channels

Top plate

Polycarbonate interior window

Polycarbonate window with glass inlay

Bottom plate

Etched-foil heater

Air gap

$2z_*$

z

x

Fire-proof drywall

Styrofoam

Polycarbonate corner support

Glass window & air gap

Figure 1: Schematic of Rayleigh Benard convection cell.

Polycarbonate interior window

Test section

Scanning mirror

ROI

Ar-ion laser

CCD β for RH110

CCD α for RHB

Filter (>570nm)

Filter (>495nm)

Beam splitter

Figure 2: Arrangement of transmitting and receiving optics. The top plate of the test section is not illustrated.

Figure 3: Fluorescent images captured by individual CCD cameras. (a)Camera α (Rhodamine B), (b) Camera β (Rhodamine 110).

Figure 4: Ratio of fluorescence intensity, (a) without blurring compensation, (b) with blurring compensation.
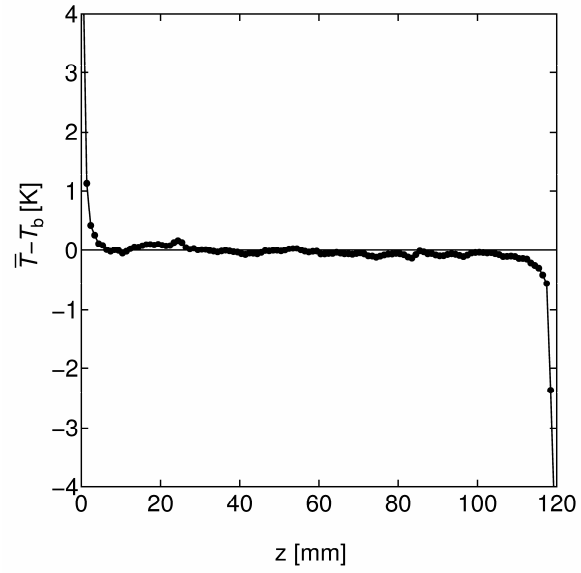
Figure 5: Fluorescence intensity distribution and their ratio across the laser light beam. Rhodamine 110 distribution is slightly wider than that of Rhodamine B.

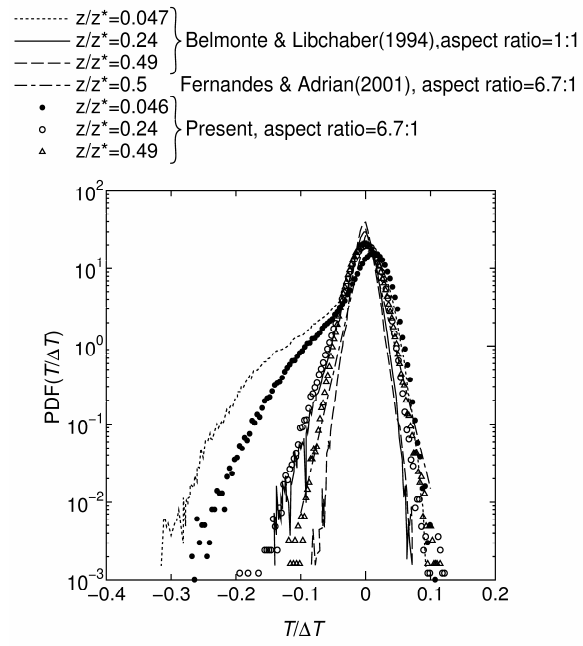Figure 6: Mean temperature (a) and RMS temperature (b) distributions.
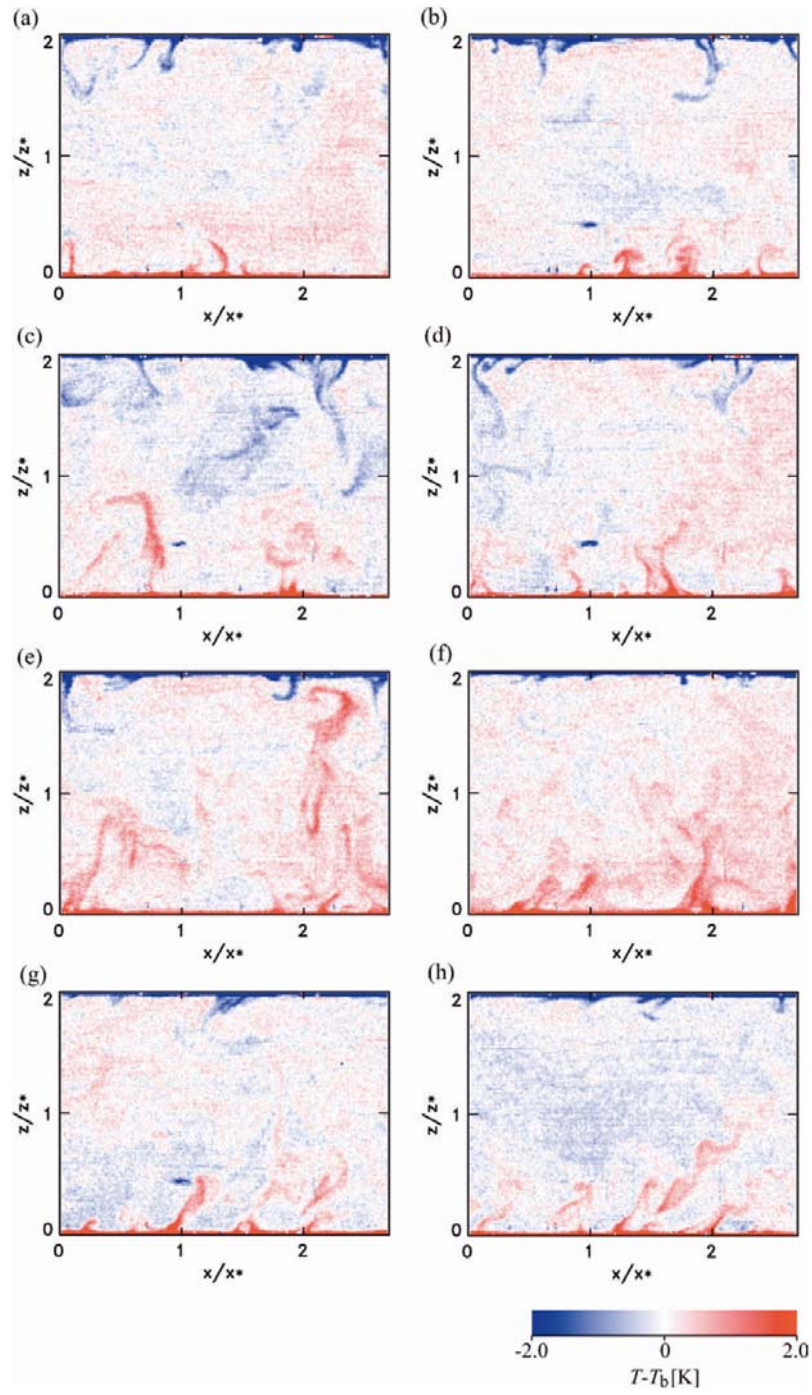
Figure 7: Probability density function for temperature.

Figure 8: Instantaneous temperature distributions.